Single-molecule DNA dynamics in tapered contraction-expansion microchannels under electrophoresis

Xin Hu,[1] Shengnian Wang,[1,*] and L. James Lee[1,2,†]

[1]*Nanoscale Science and Engineering Center for Affordable Nanoengineering of Polymeric Biomedical Devices (CANPBD), The Ohio State University, Columbus, Ohio 43210, USA*

[2]*Department of Chemical and Biomolecular Engineering, The Ohio State University, Columbus, Ohio 43210, USA*

(Received 31 December 2008; published 9 April 2009)

We investigated the dynamics of single DNA molecules driven by the electrophoretic force in several tapered contraction-expansion microchannels. Under high localized electric-field gradients, fast transition between the stretching and compression of DNA molecules was achieved. Numerically, a combination of the finite element method and the coarse-grained Brownian dynamics simulation was used to capture the dynamics of single DNA molecules simplified as freely-draining bead-spring wormlike chains. A generalized predictor-corrector time marching scheme was proposed in this work. It was found that the initial conformation, the initial center-of-mass location, and the electric-field strength are three major factors affecting the DNA dynamics. The forced relaxation due to the reverse compression in the expansion zone can speed the relaxation of DNA molecules compared with the free relaxation in the bulk. We have also simulated DNA dynamics in different contraction-expansion microchannels by changing the length or the small-end width of the contraction zone (with other geometrical lengths fixed). Decreasing the small-end width can provide higher DNA stretching due to both increased Deborah number and increased accumulated strain. Increasing the length of the contraction zone, on the other hand, only slightly increases the accumulated strain, while greatly decreases the Deborah number, causing a decrease in DNA stretching. Experimentally, DNA molecules were gradually stretched in the contraction zone and then were quickly compressed back within a short distance outside the contraction zone. DNA chains in different initial configurations demonstrate different behaviors in contraction-expansion microchannels. The Brownian dynamics simulation results are in qualitative agreement with the experimental observations.

DOI: 10.1103/PhysRevE.79.041911 PACS number(s): 87.15.hp, 87.14.gk, 83.10.Mj

I. INTRODUCTION

The dynamics of single DNA molecules in micro/nanofluidics has attracted a great deal of attention because of its importance in many biomedical applications such as DNA separation, DNA conjugation, gene mapping, and gene delivery. These applications require controlled manipulation such as moving, stretching, condensing, and packing of individual DNA molecules. There are many ways to manipulate a large number of DNA molecules at the micro/nanoscale using mechanical [1–3], hydrodynamic [4,5], electrokinetic (electro-osmotic, electrophoretic, and dielectrophoretic) forces [6,7] or their combination. Mechanical force based approaches, such as optical tweezers, magnetic tweezers, and atomic force microscopy (AFM), are suitable for stretching or twisting a single DNA molecule into different shapes, but they are difficult for large-scale multi-DNA manipulation due to high cost and complicated operation. Hydrodynamic forces work very well in many microscaled systems. However, the exerted pressure needs to increase greatly in order to keep the flow flux the same as the channel size decreases because the pressure drop in a straight rectangular channel is a reciprocal cubic function of the channel width when the fluid flux is constant, e.g., $\frac{\delta p}{L}=\frac{12\eta Q}{DW^3}$, where δp is the pressure drop, η is the viscosity, Q is the flow flux; L, D, and W are the length, depth, and width of the channel, respectively. Since most micro/nanofluidic devices are made of silicon, glass or polymer, they cannot sustain very high pressure; thus hydrodynamic forces are not applied in aqueous solutions when the channel size is small. Electrokinetic forces are attractive alternatives to the hydrodynamic and mechanical forces. One can generate different flow patterns such as extensional, rotational, and shear flows using electro-osmosis by controlling the surface charge density and type [8–10]. To move charged particles, electrophoresis can be applied without much fluid flow and this unique advantage has been utilized in many biomedical applications.

The contraction-expansion structure (either abrupt or tapered) is very common in micro/nanofluidic devices. Since the electric field $\mathbf{E}$ satisfies the divergence-free condition $\nabla\cdot\mathbf{E}=0$, its magnitude increases in the contraction zone, while decreases in the expansion zone. As we show in Fig. S.1 of the supplemental material, the tapered contraction-expansion channel can achieve higher magnitude of electric field than the abrupt counterparts at the same conditions. Thus the tapered contraction zone can be utilized to accelerate the movement of DNA molecules and stretch them in a short distance because of an increasing electric field and gradient, while the expansion zone serves as a damper to decelerate the DNA molecules and compress them back to the equilibrium state.

*Present address: Institute for Micromanufacturing, Louisiana Tech University, USA.

†Author to whom correspondence should be addressed. leelj@chbmeng.ohio-state.edu

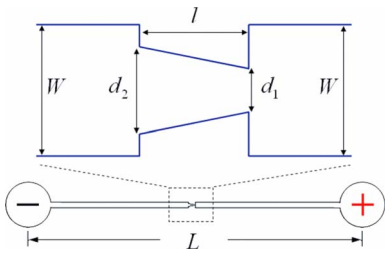

FIG. 1. (Color online) Schematics of a contraction-expansion microchannel.

DNA dynamics in either abrupt or tapered contraction-expansion channel has been studied by many researchers. By using the electrophoretic force, the "entropy trapping" method has demonstrated that the larger T2-DNA molecules move faster than the smaller T7-DNA molecules in the well-defined abrupt contraction-expansion nanoarrays [11]. The Brownian dynamics simulation has been carried out to investigate the electrophoretic migration of DNA molecules in the entropy trapping nanochannel and achieved good qualitative agreement with experimental results [12,13]. However, when the aspect ratio and the size of the entropy trap array change, the smaller λ-DNA molecules move faster than the larger T2-DNA molecules in the abrupt contraction-expansion microarray [14], indicating that this type of separation mechanism is highly size dependent and the electric-field distribution plays an important role in the DNA separation. These studies mainly concentrated on the effect of electric field on the DNA separation without considering single DNA dynamics in different zones of the channels. Experimental study and numerical simulation on DNA stretching in a nearly constant gradient of electric field produced by a hyperbolic contraction microchannel were first reported by Doyle and coworkers [15,16]. It was found that the fractional extension of DNA molecules increases with the Deborah number and it can be further increased by prestretching the DNA molecules using a gel matrix near the entry of the hyperbolic contraction microchannel. DNA dynamics in contraction microchannels with different shapes has also been studied [16], but the behavior of DNA molecules, especially the forced relaxation (or compression) in the expansion zone were not addressed. Also the effects of contraction length and small-end size on DNA stretching have not been studied.

Overall, DNA dynamics driven by the electrophoretic force in the microscaled tapered contraction-expansion channel is still not fully understood; especially the effects of geometry and electric field on DNA dynamics need to be thoroughly investigated. In this paper, we numerically studied the electrophoretic migration of DNA molecules in four tapered contraction-expansion microchannels with different length of contraction zone or width of the small end. Figure 1 shows a typical tapered contraction-expansion microchannel with the total length between two reservoirs L, the width of expansion zone W, the length of contraction zone l, the small-end width of the contraction zone d_S, and the large-end width of the contraction zone d_L. The values of L, W, and d_L are fixed, i.e., 1.5 cm, 300 μm, and 130 μm, respectively. Table I shows the lengths of contraction zones and small-end sizes of these four channels. Experimentally, we compared the effects of the initial configuration and the initial location on the dynamics of single DNA molecules in channel no. 1 with simulations.

TABLE I. Lengths and small-end sizes of four contraction channels.

Channel number	Length of contraction zone (μm)	Width of the small end (μm)
1	300	20
2	300	10
3	100	20
4	20	20

This paper is organized as follows. Section I is a brief introduction. Section II concentrates on the simulation processes of the DNA dynamics in the electrophoretically driven contraction-expansion flow. First, we propose a generalized predictor-corrector method for the bead-spring wormlike chain model under a nonuniform electric-field gradient. Second, we use the finite element method (FEM) to solve the electric field and analyze the electric-field gradient, the path-dependent Deborah numbers, and accumulated strains along different electric-field lines. Then the procedure of the Brownian dynamics simulation of single DNA molecules is given. In Sec. III, we discuss the effects of initial conformation, initial center-of-mass location, electric-field strength, and geometry of microchannels on DNA dynamics. Comparison between the simulations and experimental results is also given. Finally, the conclusion is drawn in Sec. IV.

II. SIMULATION PROCESSES

A. Brownian dynamics simulation using the bead-spring chain model

The contour length of a fluorescence-dyed λ-DNA molecule is around 21 μm, while its diameter is only 2 nm, thus the aspect ratio is up to 10^4. To simulate the conformation change of such large molecules in an affordable way, a coarse-grained approach is often used, which neglects the detailed molecular structures of DNA molecules, while captures their movement and conformation changes. This approach is the Brownian dynamics simulation (BDS) and has been successfully used in the simulation of single DNA dynamics in both hydrodynamically and electrophoretically driven flows [17–23].

In this study, we use the bead-spring chain model to simulate DNA dynamics. A bead-spring λ-DNA chain consists of $N=20$ beads connected by $N_S=N-1=19$ elastic springs. There are $N_K=N_{K,S}N_S=152$ total Kuhn steps in one chain with $N_{K,S}=8$ Kuhn steps in each spring. The contour length of a labeled DNA is $L_C=N_K b_K=21$ μm, where $b_K=0.138$ μm is the length of one Kuhn step. The hydrodynamic interaction between DNA segments and the solid wall is neglected in this study either because its contribution is small or its effect can be partially included by using an "effective" drag coefficient [24,25]. The final dimensionless governing equation is given as

$$\frac{d\mathbf{r}_i}{dt} = \mathrm{Pe}_1\mathbf{u}_i + \mathrm{Pe}_2\mathbf{E}_i + \mathbf{f}_i^r + \mathbf{f}_i^{s,\mathrm{total}}, \tag{1}$$

where coordinates, time, velocity and electric fields are nondimensionalized by $b=\sqrt{N_{K,S}}b_K$, $\xi N_K b_K^2/k_BT$ (which is the characteristic time), the characteristic velocity U_{ref}, and characteristic electric-field strength E_C, respectively. In this paper, ξ is the drag coefficient for one bead. $E_C=\delta\phi/d_S$, where $\delta\phi$ is the potential difference between two reservoirs. Both $\mathrm{Pe}_1=\frac{U_{\mathrm{ref}}}{(k_BT)/(b\xi)}$ and $\mathrm{Pe}_2=\frac{\mu_{\mathrm{EP}}E_C}{(k_BT)/(b\xi)}$ are the parameters defining the ratio of characteristic flow (either hydrodynamic or electrophoretic) velocity to bead diffusion velocity, or the ratio of the bead diffusion time to the characteristic flow time (thus they are similar to the Péclet number in a convection-diffusion partial differential equation). $\mu_{\mathrm{EP}}=q/\xi$ is the DNA EP mobility and q is the charge density for each bead. The dimensionless Brownian force is $\mathbf{f}_i^r=\sqrt{6/\Delta t}\mathbf{n}_i$, where $\mathbf{n}_i$ is a three-dimensional (3D) uniform random number in $[-1,1]$. In the simulation, we select an initial seed and use a pseudo-random number generator to generate a 3D random number vector for $\mathbf{n}_i$ at different time step, thus all these 3D random number vectors form a series with the same seed. The selection of the initial random seed is associated with the chain number since different chains have different chain numbers or initial conformations. Thus in the simulation, different chains have different Brownian forces even if their initial center-of-mass locations are the same. The dimensionless total spring force on bead i is given by $\mathbf{f}_i^{s,\mathrm{total}}=\mathbf{f}_i^s-\mathbf{f}_{i-1}^s$ with the ith spring force satisfies the wormlike chain (WLC) model [26,27], $\mathbf{f}_i^s=\vartheta(\frac{1}{2\lambda_i(1-\lambda_i)^2}-\frac{1}{2\lambda_i}+2)(\mathbf{r}_{i+1}-\mathbf{r}_i)$, where $\lambda_i=|\mathbf{r}_{i+1}-\mathbf{r}_i|/\sqrt{N_{K,S}}$, $\vartheta=b_K/(2\lambda_p^{\mathrm{eff}})$, and λ_p^{eff} is the "effective" persistence length [18]. For a DNA chain with 20 beads, we use $N_{K,S}=8$, $\lambda_p^{\mathrm{eff}}=0.096$ μm, $b_K=0.132$ μm, and $\vartheta=0.6875$.

Equation (1) can be explicitly rewritten as

$$d\mathbf{r}_i = (\mathrm{Pe}_1\mathbf{u}_i + \mathrm{Pe}_2\mathbf{E}_i)dt + (\mathbf{f}_i^s - \mathbf{f}_{i-1}^s)dt + \mathbf{f}_i^r dt, \tag{2}$$

which is a time evolution equation and needs to be solved using a time integration (or time marching) method. Because each spring has a maximum extensibility in the wormlike chain model, the conventional marching schemes such as the forward Euler's method or midpoint method cannot guarantee that the length of each spring will never exceed its maximum unless a very small time step size is used. To avoid this physical discrepancy, a multi-predictor-corrector method has been developed for the flow with a constant velocity gradient tensor [28]. Here, we modified this method and extended it to the more general case where the gradient of the velocity or the electric field is no longer constant. The main idea is first to predict the movement of the center of mass of a chain using the fourth-order Runge-Kutter method, then to use the calculated spring vectors to determine each bead location and update the flow and electric fields at each bead location. The procedures are given as follows [29]:

(i) Calculation of the movement of the center of mass of a chain

The movement of the center of mass $\mathbf{r}_C=\frac{1}{N}\sum_{i=1}^N\mathbf{r}_i$ is governed by

$$d\mathbf{r}_C = [\mathrm{Pe}_1\mathbf{u}(\mathbf{r}_C) + \mathrm{Pe}_2\mathbf{E}(\mathbf{r}_C)]dt + \frac{1}{N}\sum_{i=1}^N \mathbf{f}_i^r dt. \tag{3}$$

Since Eq. (3) is an independent equation, we can use the fourth-order Runge-Kutta method to calculate the location of the center of mass at time $n+1$.

(ii) Predictor steps

We have the following equation for the ith spring vector $\mathbf{R}_i$:

$$d\mathbf{R}_i = \mathrm{Pe}_1(\mathbf{u}_{i+1}-\mathbf{u}_i)dt + \mathrm{Pe}_2(\mathbf{E}_{i+1}-\mathbf{E}_i)dt + (\mathbf{f}_{i+1}^s - 2\mathbf{f}_i^s + \mathbf{f}_{i-1}^s)dt + (\mathbf{f}_{i+1}^r - \mathbf{f}_i^r)dt. \tag{4}$$

The forward Euler method used to get its predicted value $\mathbf{R}_i^{(p)}$,

$$\mathbf{R}_i^{(p)} = \mathbf{R}_i^{(n)} + \mathrm{Pe}_1[\mathbf{u}(\mathbf{r}_{i+1}^{(n)}) - \mathbf{u}(\mathbf{r}_i^{(n)})]dt + \mathrm{Pe}_2[\mathbf{E}(\mathbf{r}_{i+1}^{(n)}) - \mathbf{E}(\mathbf{r}_i^{(n)})]dt + (\mathbf{f}_{i+1}^{s(n)} - 2\mathbf{f}_i^{s(n)} + \mathbf{f}_{i-1}^{s(n)})dt + (\mathbf{f}_{i+1}^{r(n)} - \mathbf{f}_i^{r(n)})dt, \tag{5}$$

where $\mathbf{R}_i^{(n)}$ and $\mathbf{f}_i^{s(n)}$ are the ith spring vector and spring force at time step n, and $\mathbf{f}_i^{r(n)}$ is the Brownian force for the ith bead at time step n.

It can be easily shown that $N\mathbf{r}_1=N\mathbf{r}_C-\mathbf{R}_{N-1}-2\mathbf{R}_{N-2}-\cdots-(N-2)\mathbf{R}_2-(N-1)\mathbf{R}_1$. Thus we can obtain the intermediate location of each bead at the predictor step as follows:

$$\begin{cases} \mathbf{r}_1^{(p)} = \mathbf{r}_C^{(n+1)} - \frac{1}{N}\sum_{k=1}^{N-1} k\mathbf{R}_{N-k}^{(p)} \\ \mathbf{r}_2^{(p)} = \mathbf{r}_1^{(p)} + \mathbf{R}_1^{(p)} \\ \cdots \quad \cdots \quad \cdots \\ \mathbf{r}_N^{(p)} = \mathbf{r}_{N-1}^{(p)} + \mathbf{R}_{N-1}^{(p)} \end{cases}. \tag{6}$$

(iii) First corrector step

If we remove the term associated with the spring force in spring i to the left-hand side of Eq. (4), we can calculate the corrected spring length through the following equation:

$$\mathbf{R}_i^{(c1)} + 2\mathbf{f}_i^{s(c1)}dt = \mathbf{R}_i^{(n)} + \mathrm{Pe}_1\left[\mathbf{u}\left(\frac{\mathbf{r}_{i+1}^{(p)}+\mathbf{r}_{i+1}^{(n)}}{2}\right) - \mathbf{u}\left(\frac{\mathbf{r}_i^{(p)}+\mathbf{r}_i^{(n)}}{2}\right)\right]dt + \mathrm{Pe}_2\left[\mathbf{E}\left(\frac{\mathbf{r}_{i+1}^{(p)}+\mathbf{r}_{i+1}^{(n)}}{2}\right) - \mathbf{E}\left(\frac{\mathbf{r}_i^{(p)}+\mathbf{r}_i^{(n)}}{2}\right)\right]dt + (\mathbf{f}_{i+1}^{s(n)} + \mathbf{f}_{i-1}^{s(c1)})dt + (\mathbf{f}_{i+1}^{r(n)} - \mathbf{f}_i^{r(n)})dt, \tag{7}$$

where $\mathbf{R}_i^{(c1)}$ and $\mathbf{f}_i^{s(c1)}$ are ith spring vector and spring force in the first corrected step. The term $\mathbf{f}_{i-1}^{s(c1)}$ on the right-hand side is known because we can sweep the index i from 1 to $N-1$. For beads 1 and N, there is only one spring force on the right-hand side. Equation (7) can be transferred to a cubic equation on $\lambda_i=R_i^{(c1)}/\sqrt{N_{K,S}}$ and there is only one root of λ_i in (0, 1). After solving it, we can get the first corrected ith spring length vector $\mathbf{R}_i^{(c1)}$. Using the similar method mentioned above, we can figure out the first corrected location $\mathbf{r}_i^{(c1)}$ for bead i.

(iv) Second corrector step

The second corrector step similar to the first corrector step except for some terms on the right-hand side of the equation:

$$\mathbf{R}_i^{(c2)} + 2\mathbf{f}_i^{s(c2)}dt = \mathbf{R}_i^{(n)} + \mathrm{Pe}_1\left[\mathbf{u}\left(\frac{\mathbf{r}_{i+1}^{(c1)} + \mathbf{r}_{i+1}^{(n)}}{2}\right) - \mathbf{u}\left(\frac{\mathbf{r}_i^{(c1)} + \mathbf{r}_i^{(n)}}{2}\right)\right]dt + \mathrm{Pe}_2\left[\mathbf{E}\left(\frac{\mathbf{r}_{i+1}^{(c1)} + \mathbf{r}_{i+1}^{(n)}}{2}\right) - \mathbf{E}\left(\frac{\mathbf{r}_i^{(c1)} + \mathbf{r}_i^{(n)}}{2}\right)\right]dt + (\mathbf{f}_{i+1}^{s(c1)} + \mathbf{f}_{i-1}^{s(c2)})dt + (\mathbf{f}_{i+1}^{r(n)} - \mathbf{f}_i^{r(n)})dt, \quad (8)$$

where $\mathbf{R}_i^{(c2)}$ and $\mathbf{f}_i^{s(c2)}$ are ith spring vector and spring force in the second corrected step. Using a similar method mentioned in the first corrector step, we can figure out the second corrected spring vector $\mathbf{R}_i^{(c2)}$ and location $\mathbf{r}_i^{(c2)}$ for bead i.

(v) Checking step

We need to check whether the residual condition $\delta = \sqrt{\sum_{i=1}^{N-1}|\mathbf{R}_i^{(c2)} - \mathbf{R}_i^{(c1)}|^2} < \delta_0$ is satisfied, where $\delta_0 = 10^{-6}$ is the prescribed criteria for the error in this study. If this condition is satisfied, we let $\mathbf{R}_i^{(n+1)} = \mathbf{R}_i^{(c2)}$ and begin the next time step; if it is not satisfied, then we let $\mathbf{R}_i^{(c1)} = \mathbf{R}_i^{(c2)}$, $\mathbf{r}_i^{(c1)} = \mathbf{r}_i^{(c2)}$ and repeat steps (iv) and (v) again until the residual condition is satisfied.

In electrokinetic flow, it is extremely difficult to remove the effect of electro-osmotic flow (EOF) and keep the electrophoresis unaffected at the same time. Some researchers suggested using polyvinylpyrrolidone (PVP) to suppress or screen the effect of EOF [15]. However, we found that the adding of PVP also lowers down the electrophoretic mobility of DNA molecules. It might be because PVP is positively charged and thus it also binds to DNA molecules as it does to the negatively charged surfaces of microfluidic devices. In this study, the contribution of EOF to DNA dynamics, in fact, is negligible because the large amount of ions in the DNA buffer solution can suppress the EOF as mentioned in [30,31]. Thus there is only one Péclet number $\mathrm{Pe} = \mathrm{Pe}_2 = \frac{\mu_{\mathrm{EP}} E_C}{(k_B T)/(b\xi)}$, from the contribution of electrophoretic flow. The characteristic electric-field strength $E_C = \delta\phi/d_S$ can be determined from the experiment with the known external voltage drop $\delta\phi$ and the width of small end of the contraction zone d_S. The drag coefficient of single bead is given by $\xi = \xi_{\mathrm{tot}}/N$, where ξ_{tot} is the total drag coefficient for a DNA chain. The value of $\mu_{\mathrm{EP}} = q/\xi$ depends on the charge density of a DNA bead, which is affected by the composition of the buffer solution (such as pH value). In the simulation, we set $\mathrm{Pe} = -21000$ in order to achieve a quantitative agreement with experiment observations at a voltage drop $\delta\phi = 100$ V. Other values $\mathrm{Pe} = -42000$ and -84000 were also chosen to study how the magnitude of electric field affects DNA dynamics.

B. Simulation of electric field in the contraction-expansion microchannel

It has been observed in our previous work that the electric field away from the reservoirs in a microfluidic channel is nearly two dimensional [7,9]. Thus we can neglect the electric-field component in the depth direction and only solve for the 2D electric field in the contraction microchannel. The dimensionless electric potential ϕ is governed by the Laplace equation $\nabla^2\phi = 0$ and the dimensionless electric field is given by $\mathbf{E} = -\nabla\phi$, where the electric potential, the length, and the electric field are nondimensionalized by $\delta\phi$, d_S, and $E_C = \delta\phi/d_S$, respectively. The dimensionless electric potential is set to 0 at the inlet reservoir and 1 at the outlet reservoir. The neutral condition $\mathbf{n}\cdot\nabla\phi = 0$ is prescribed on the wall surface. We use the FEM to solve the governing equation with the following weak form:

$$\left\{\int_{\Omega_e} \nabla N_i \cdot \nabla N_j d\Omega\right\}\{\phi_j\} = 0, \quad (9)$$

where N_i and N_j are the interpolation functions. The bilinear interpolation is used for the electric potential at the nodal points. The electric field is first calculated at the element level, and then we use the least-squares fitting method to get the smooth values at the nodal points [29]:

$$\left[\int_{\Omega_e} N_i N_j d\Omega\right]\{\mathbf{E}_j\} = \int_{\Omega_e} N_i \mathbf{E}^{(e)} d\Omega. \quad (10)$$

The whole geometry is discretized by the structured mesh (four-noded bilinear quadrilateral elements), which is automatically generated in the source code. The mesh density affects the accuracy of the calculated potential and electric field, especially at the location where the gradient is large. It is well known that for Laplace equation, the bilinear interpolated finite element solution ω^h satisfies $\|\omega^h - \omega^*\|_0 \le C_1 h^2 \|\omega^*\|_2$, where ω^* is the exact solution, h is the maximum mesh size, and $\|\cdot\|_0$ and $\|\cdot\|_2$ are the ℓ_0 and ℓ_2 norm [32]. Thus increasing the mesh density can quadratically minimize the maximum relative error from the finite element discretization. In this study, we kept on doubling the element number (mesh density) until the maximum relative error $\|\omega^{h/2} - \omega^h\|_0 / \|\omega^h\|_0$ is less than 0.1%.

Since the structured mesh is automatically generated, we know exactly the layout of nodes and elements. Thus the electric field at any location can be easily interpolated without using the neighbor-to-neighbor or Octree search [33] in the entire domain.

C. Analysis of the effect of electric field on DNA dynamics

In order to better analyze the effect of electric field on DNA dynamics, we select channel no. 1 as an example and pick four dimensionless locations (x_0, y_0, and z_0) as the starting points of the center of mass of DNA chains. Here we fix $x_0 = -4.9$ where the electric field nearly constant. Also the value of $z_0 = 0$ is prescribed since the electric field is nearly two dimensional. The y components of the starting points are chosen as $y_0 = 0$, 1.05, 2.1, and 3.15. The electric-field lines (denoted as A, B, C, and D) passing these four starting points are shown in Fig. 2(a).

The movement of the ith bead relative to that of the center of mass of a chain can be described by the following equation:

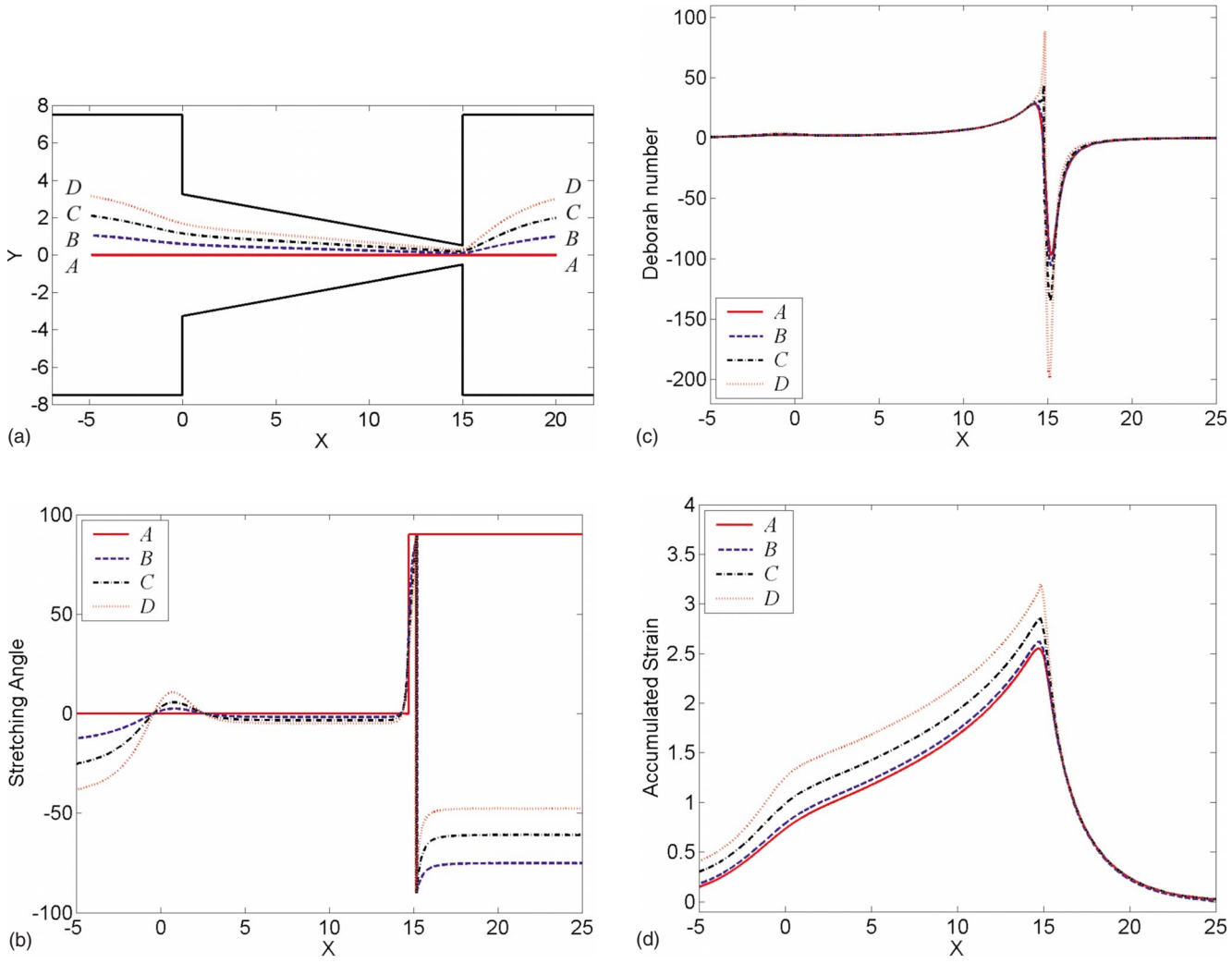

FIG. 2. (Color online) (a) Four starting points and the electric-field lines for studying the DNA dynamics in the contraction-expansion microchannel; (b) change in the stretching angle, distributions of (c) location-dependent Deborah number and (d) path-dependent accumulated strain vs x-axis coordinate along the four electric-field lines.

$$\frac{d}{dt}(\mathbf{r}_i - \mathbf{r}_C) = (\mathbf{f}_i^{s,\text{total}} + \mathbf{f}_i^r) - \frac{1}{N}\sum_{i=1}^{N} \mathbf{f}_i^r + \text{Pe}\,\nabla\mathbf{E}(\mathbf{r}_C)\cdot(\mathbf{r}_i - \mathbf{r}_C). \tag{11}$$

Thus the conformation change of a DNA chain (i.e., the left-hand side term) is mainly determined by the electric-field gradient $\text{Pe}\nabla\mathbf{E}$. Since the electric field $\mathbf{E}$ satisfies $\nabla\cdot\mathbf{E}=0$ and $\nabla\times\mathbf{E}=0$, the electric-field gradient tensor $\nabla\mathbf{E}$ is a symmetric positive definitive tensor, i.e., $\nabla\mathbf{E} = \begin{pmatrix} \alpha & \beta \\ \beta & -\alpha \end{pmatrix}$, where $\alpha=\frac{\partial E_x}{\partial x}$ and $\beta=\frac{\partial E_x}{\partial y}$. Thus the movement of a charged particle or polyelectrolyte in the electric field is still extensional although the electric-field gradient tensor is not constant [27]. Matrix $\text{Pe}\nabla\mathbf{E}$ has two eigenvalues: $\lambda_1=\text{Pe}\sqrt{\alpha^2+\beta^2}$ (associated with stretching) and $\lambda_2=-\text{Pe}\sqrt{\alpha^2+\beta^2}$ (associated with compression). For $\beta=0$, the corresponding stretching and compression eigenvectors (directions) are (1,0) and (0,1) if $\alpha>0$, or (0,1) and (1,0) if $\alpha<0$. For $\beta\neq 0$, the corresponding stretching and compression eigenvectors (directions) are $(1, \tan\theta)$ and $[1, \tan(\theta+\pi/2)]$, where $\tan\theta=(\sqrt{\alpha^2+\beta^2}-\alpha)/\beta$ and $-\pi/2<\theta\leq\pi/2$. This indicates that the stretching direction makes an angle θ with the x axis and the compression direction is forming an angle of $\theta+\pi/2$ with the x axis. Also the stretching or compression direction is independent on the value of the Péclet number.

Since the electric field and its gradient have been calculated by FEM, we can easily get the relation of stretching angle (in degree) vs the x component of the field lines, which is plotted in Fig. 2(b). We can see that the stretching angle changes suddenly from 0° (in the x axis direction) to 90° (in the y axis direction) near the small end along the electric-field line A. This indicates that DNA molecules are stretched along the x axis and compressed along the y axis in the contraction zone, while they are stretched along the y axis and compressed along the x axis in the expansion zone. The stretching angles along the other three electric-field lines are not constant, but they also experience a sudden change near the small end of the contraction zone.

In a 2D pure extensional hydrodynamic flow, the average stretching of DNA molecules is related to the Deborah number defined as $\text{De}=\tau_{\text{relax}}\dot{\varepsilon}$, where τ_{relax} is the longest relax-

ation time for DNA chains and $\dot{\varepsilon}$ is the extensional rate [18,19]. Similarly, we can also study the behavior of DNA chains at different "electrophoretic" Deborah number since the electrophoretic motion is still extensional. Due to the non-uniform electric field, we can expect that the "electrophoretic" Deborah number is not constant in the whole microfluidic device. Using the same definition as the hydrodynamic flow, the local dimensional electrophoretic velocity field $\mu_{\mathrm{EP}}E_C\mathbf{E}$, or $\mathrm{Pe}\frac{k_BT}{b\xi}\mathbf{E}$, can be transformed to matrix $d_S\left(\begin{smallmatrix}\dot{\varepsilon} & 0\\ 0 & -\dot{\varepsilon}\end{smallmatrix}\right)\cdot\left(\begin{smallmatrix}\tilde{x}\\ \tilde{y}\end{smallmatrix}\right)$ after coordinate transformation, where $(\tilde{x},\tilde{y})$ is dimensionless local coordinates and d_S is the characteristic length or the small-end size of the contraction zone. Since DNA molecules experience stretching in the contraction area and compression in the expansion area, we have the dimensional localized extensional (or compression) rate $\dot{\varepsilon}=\frac{\mathrm{Pe}}{d_S}\frac{k_BT}{b\xi}\|\nabla\mathbf{E}\|_2\,\mathrm{sgn}(\alpha)$, where $\|\cdot\|_2$ is the ℓ_2 norm of a matrix, $\|\nabla\mathbf{E}\|_2=\sqrt{\alpha^2+\beta^2}$, and $\mathrm{sgn}(\cdot)$ is the sign function (positive for extension and negative for compression). Thus the Deborah number $\mathrm{De}=\tau_{\mathrm{relax}}\frac{\mathrm{Pe}}{d_S}\frac{k_BT}{b\xi}\|\nabla\mathbf{E}\|_2\,\mathrm{sgn}(\alpha)$ is proportional to the Péclet number Pe, or the strength of electric field and is path dependent.

For Pe=−21000, we plot the location-dependent Deborah number vs the center-of-mass location along the electric-field lines *A*, *B*, *C*, and *D* in Fig. 2(c). We can see that the location-dependent Deborah number first gradually reaches its maximum value before approaching the small end of the contraction zone (dimensionless location $x=15$) and then rapidly decreases to the negative minimum value. This means that the electric-field gradient has already exerted a reverse compressive force to DNA chains before they exit the small end of the contraction zone. The fact that the absolute value of the maximum compression Deborah number is larger than that of the maximum stretching Deborah number indicates that the speed of compression is higher than that of stretching. With the electric-field gradient diminishes along the expansion channel, the location-dependent Deborah number approaches 0, showing that DNA chains are back to the equilibrium state. The maximum stretching Deborah number is achieved along the electric-field line *D*, the one closest to the wall.

The maximum stretching length of DNA chains also depends on the accumulated strain ε, which has been used to describe the deformation rate of an object and can be written as $\varepsilon=\int_{\mathrm{path}}\dot{\varepsilon}dt=\int_{\mathrm{path}}\frac{\dot{\varepsilon}}{\mu_{\mathrm{EP}}E_C|\mathbf{E}|}ds$, where s is the dimensional curve length of an electric-field line or path [15,16]. We have $\varepsilon=\int_{\mathrm{path}}\mathrm{sgn}(\alpha)\frac{\|\nabla\mathbf{E}\|_2}{|\mathbf{E}|}d\tilde{s}$, where $\tilde{s}$ is the dimensionless curve length. Since the formula only contains the dimensionless variables along the given path and does not include the controlling parameter Pe, the accumulated strain is only path dependent. We plot the accumulated strain along the electric-field lines *A*, *B*, *C*, and *D* in Fig. 2(d). The accumulated strain gradually increases to its maximum value near the small end of the contraction area, then decreases to zero in the expansion area. The four accumulated strain curves overlap with one another in the expansion zone indicating that the deformation of DNA chains in the expansion zone is almost the same and unrelated to their upstream locations.

D. Procedures of the simulation of DNA dynamics

The simulation procedures of the fluorescence-dyed λ-DNA dynamics in the contraction-expansion microchannel are given as follows:

(1) Import the FEM simulation results of the electric field into the Brownian dynamics simulation. Since the constructed mesh is generated automatically in source code, we know the exact location of any given element or node and it is easy to find out the element number where a bead is located. Then the electric field at any bead location can be easily interpolated.

(2) Calculate the three-dimensional equilibrium distribution of 100 bead-spring wormlike chains and store their equilibrium distribution in a file to be read in the next step.

(3) Simulate the DNA dynamics driven by the electrophoresis in the contraction-expansion microchannel by setting the values for the controlling parameter Pe and the initial center-of-mass location of DNA chains. The dimensionless time step Δt is chosen as 1×10^{-5} for Pe=−84000, and 2×10^{-5} for other two electric-field strengths. However, the total time step n for each simulation is required to satisfy the condition $n\Delta t\cdot\mathrm{Pe}=-1.6\times10^{7}$.

III. SIMULATION RESULTS AND DISCUSSION

A. Effect of the initial configuration

For a DNA chain moving in nonuniform electric field, it is important to study the change in the fractional visual length (the maximum distance between the beads vs the contour length) with its center-of-mass location. Figure 3(a) shows such curves for 100 individual DNA chains (the dash lines) and their ensemble average (the solid bold line) along the electric field line *A* at Pe=−21000. We can see that different DNA chains experience different coil-stretching-compression histories although their initial center-of-mass locations are the same. This nonuniformity is due to the difference in the initial chain conformation [16]. After ensemble averaging the effect of the initial conformation, we find that the maximum averaged fractional visual length is only around 0.24, i.e., the averaged stretching length of DNA chains is around 5 μm although some DNA chains can be stretched to 13 μm.

The effect of the initial configuration to DNA dynamics can also be viewed in Fig. 3(b), which shows the movement and conformation change of two DNA chains at the same dimensionless time series [0; 10; 14.1; 17; 26]. The unit length in Fig. 3(b) stands for 20 μm, but the size of a DNA chain is enlarged 10 times for better view. These two DNA chains have the same initial center-of-mass location and the electric-field strength Pe=−21000, but different initial configuration. The symbols are used to label the center–of-mass location of DNA chains at the same time. Those symbols overlap with each other indicating that the speeds of DNA chains are the same because of the same starting point. Both DNA chains are stretched and aligned in the *x*-axis direction in the contraction zone, but change their alignment in the *y*-axis direction in the expansion zone. Although both experience the same coil-stretching-recoil transition in the contraction-expansion channel, they display quite different

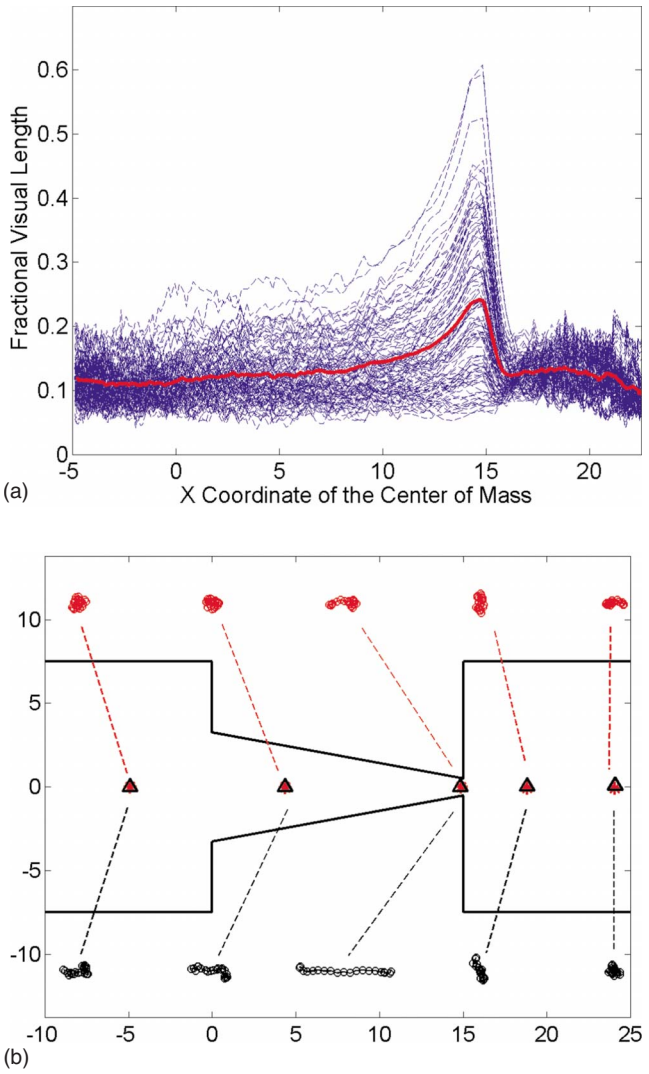

FIG. 3. (Color online) (a) The fractional visual length of 100 DNA chains and their ensemble average vs the center-of-mass locations in the contraction-expansion channel at the electric-field strength Pe=−21000; (b) effect of initial configuration to the dynamics of two DNA chains at the same initial location (on electric-field line *A*) and electric-field strength.

behavior. The top DNA chain is initially in the coiled shape, while the bottom one is partially stretched initially. It is much more difficult to stretch a coiled DNA because the magnitude of $\mathrm{Pe}\nabla\mathbf{E}(\mathbf{b}_C)\cdot(\mathbf{b}_i-\mathbf{b}_C)$ is smaller than that of an elongated chain at the same electric-field gradient. A longer DNA chain has larger value of $|\mathrm{Pe}\nabla\mathbf{E}(\mathbf{b}_C)\cdot(\mathbf{b}_i-\mathbf{b}_C)|$, thus it can be more easily stretched as shown in Fig. 3(b). We can also see that both DNA chains are compressed in the *x*-axis direction and stretched along the *y* axis in the expansion zone. Finally, both of them revert back to the coiled states in the expansion zone, but in different shapes from their initial upstream configurations.

B. Effect of the initial location

Another important aspect to be studied is the effect of the initial location on DNA dynamics. From Figs. 2(c) and 2(d), along electric-field lines *A*, *B*, *C*, and *D*, we know that the maximum stretching Deborah numbers are 28, 29, 44, and 88, respectively, and the maximum accumulated strains are 2.55, 2.62, 2.86, and 3.2, respectively. Thus, we would expect the largest stretching along the electric-field line *D* and the smallest stretching along the electric-field line *A*. This is confirmed by Fig. 4(a), which compares averaged fractional visual lengths along the four electric-field lines *A*, *B*, *C*, and *D* at Pe=−21000. We can see that the maximum averaged fractional visual length along the electric-field line *D* is around 0.255, while that along the electric-field line *A* is approximately 0.24. Thus the difference of the maximum averaged fractional visual length along two electric-field lines is around 6.25%. A similar phenomenon occurs at a higher electric-field strength Pe=−84000, where the difference of the maximum averaged fractional visual length along the two electric-field lines *A* and *D* is around 12%.

We also observe that the averaged fractional visual length slightly increases after the large drop outside the small end of the contraction zone. This slight lift-up can be attributed to the fact that the absolute value of the maximum compression Deborah number is larger than that of the stretching Deborah number as shown in Fig. 2(c). In the contraction zone, the visual length increases since DNA is stretched along the *x* axis, thus it drops greatly outside the small end of the contraction zone because of the compression along the *x* axis. Although the DNA size along the *y* axis is increasing due to the stretching along the *y* axis, it is still less than the length along the *x* axis until the visual length reaches its minimum value. At this moment, DNA length along the *x* axis is the same as that along the *y* axis. Then the overcompression along the *x*-axis direction makes the DNA length along the *y* axis longer than that along the *x* axis. Thus stretching along the *y* axis would increase the visual length at the beginning of the expansion zone. Since the compression Deborah number recedes to zero very quickly, eventually the DNA chains relax back to their equilibrium state with smaller visual lengths.

Figure 4(b) compares the dynamics of two DNA chains with the same initial configuration, but at different initial locations: one along the electric-field line *A* at the time series [0; 10; 14.1; 17; 26] and the other one along the electric-field line *D* at time [0; 10.8; 14.9; 19.2; 29.5] in order to assure that they have the same *x* component of the center-of-mass location x_C. We can see that these two DNA chains display almost the same conformation at the same value of x_C except at the small end of the contraction zone where the DNA chain along the electric-field line *D* lifts up in order to follow the electric-field line.

Although the effect of the initial *y* location on the DNA dynamics is weak compared to the effect of the initial configuration, it does affect the speed of a DNA chain. Figure 4(c) shows the conformation of two DNA chains with the same initial configuration, at the same time series [0; 10; 14.1; 17; 26], and under the same electric-field strength (Pe =−21000), but at different initial *y* locations (i.e., along electric-field lines *A* and *D*, respectively). After the same period of time, we can see that the DNA chain along the electric-field line *A* moves faster than that along the electric-field line *D*. Since we use the same random series (i.e.,

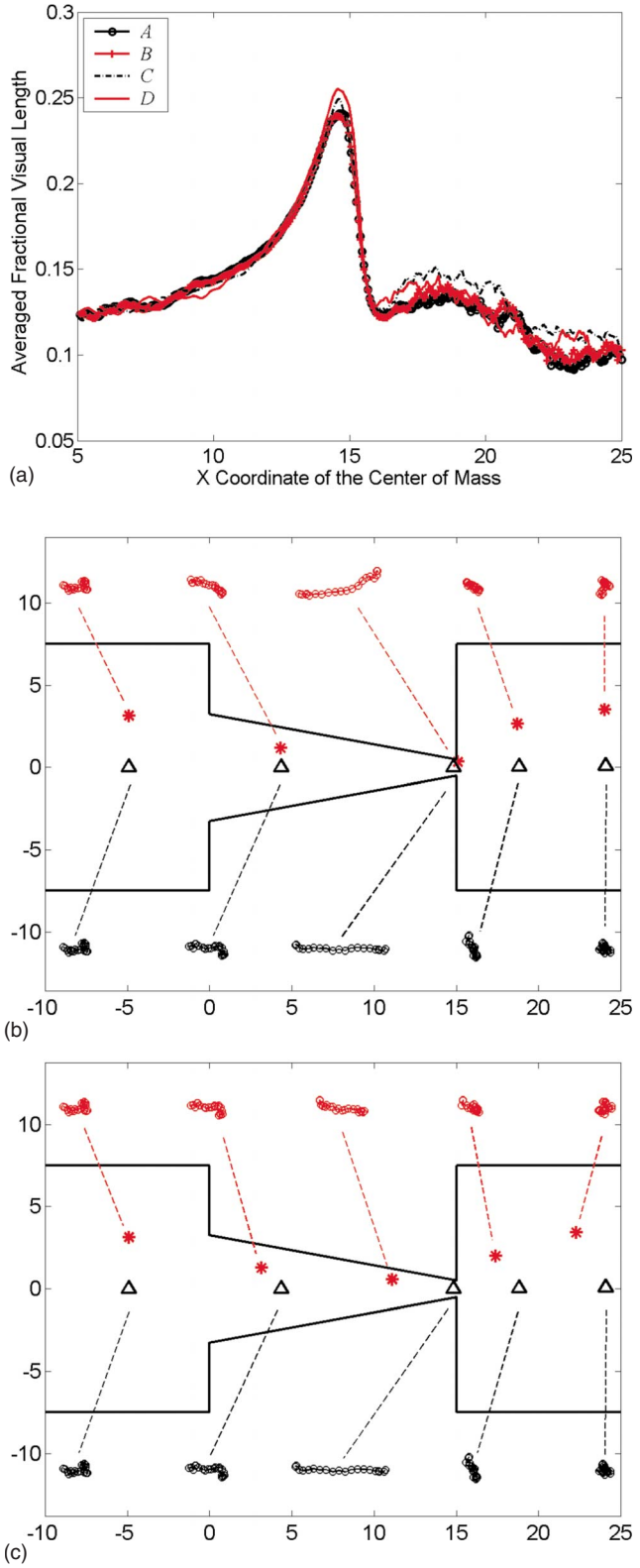

FIG. 4. (Color online) (a) The averaged fractional visual length vs the center-of-mass locations in the contraction-expansion channel along the four electric-field lines at the electric-field strength Pe=−21000; (b) dynamics of two DNA chains along electric-field lines *A* and *D* with the same *x*-axis coordinates and electric-field strength; (c) dynamics of two DNA chains along electric-field lines *A* and *D* with the same time series and electric-field strength;

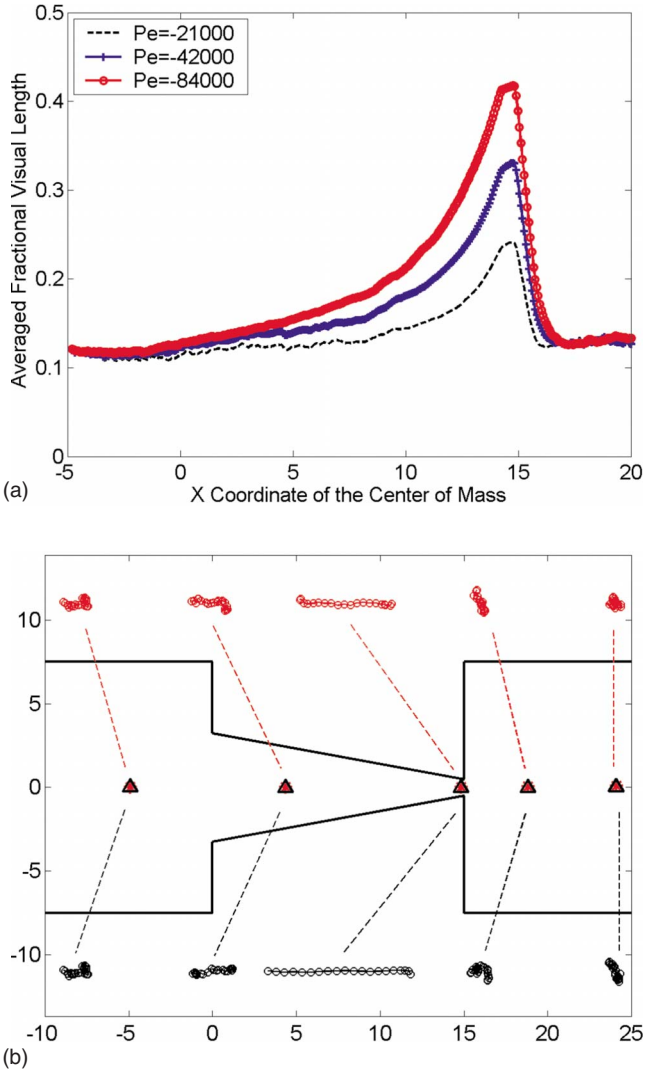

FIG. 5. (Color online) (a) The averaged fractional visual length vs the center-of-mass locations in the contraction-expansion channel along the electric-field line *A* at three different electric-field strength Pe=−21000, −42000, and −84000; (b) dynamics for two DNA chains with the same initial configuration and *x*-axis coordinates but at different electric-field strength Pe=−21000 and −84000.

Brownian force) for these two DNA chains, the difference of the center-of-mass location in the *x* axis can be described by $\delta x_C = \int_0^t \mathrm{Pe}\,\delta E_x[x_C(t')]dt'$, where δE_x is the difference of E_x along two electric-field lines. Because δE_x is positive in most region of the contraction-expansion channel and the dimensionless time period is large, we can see the obvious speed difference.

C. Effect of the electric-field strength

The effect of the electric-field strength on DNA dynamics is also very important. The larger electric-field strength provides a higher Deborah number to achieve longer stretching as confirmed in Fig. 5(a). Each curve is the averaged fractional visual length of 100 DNA chains at the same initial center-of-mass location (i.e., all along electric-field line *A*)

but with different electric-field strengths. We can see that the maximum stretching is achieved inside the contraction zone and the largest stretching (with the maximum averaged fractional visual length 0.42) is obtained at Pe=−84000. There is a substantial difference between the maximum visual lengths at these three different electric-field strengths. Thus the effect of electric-field strength to DNA dynamics is much stronger compared with the effect of the initial center-of-mass location.

Figure 5(b) shows the dynamics of two DNA chains with the same initial conformation and initial location, but at two different electric-field strengths Pe=−21000 and Pe=−84000. In order to assure that they have the same x component of the center-of-mass location x_C, the DNA chain at the lower electric strength takes a larger time series [0; 10; 14.1; 17; 26] and the other one takes only one-fourth of the previous value, i.e., a time series [0; 2.5; 3.525; 4.25; 6.25]. We can see that DNA chains can be stretched longer under larger electric-field strength.

D. Effect of geometries—length and small-end width of the contraction zone

The maximum values of Deborah number and the accumulated strain are two key factors to determine the stretching of DNA molecules. Once the external electric-field strength and the total channel length L are fixed, there might be two ways to increase the maximum stretching of DNA chains in the contraction zone. One is to shorten the width of the small end d_S while maintain the length of the contraction zone l and the width of the large end d_L. This would increase the strength of the electric-field gradient so that the maximum Deborah number also increases. The other way is to lengthen the contraction zone while keep the widths of the small end d_S and the large end d_L constant. This can raise the accumulated path-dependent strain because the effective length of path is augmented.

To examine the effects of length and small-end width of contraction zone on DNA dynamics, we plot the Deborah number and the accumulated strain along the central lines of four different contraction-expansion microchannels (detailed data are given in Table I) in Figs. 6(a) and 6(b). It demonstrates that channel no. 2 achieves the highest values for both Deborah number and the accumulated strain. This is because it obtains the highest electric-field gradient with the smallest small-end width. For other channels, it is found that the maximum Deborah number increases with decreasing the length of the contraction zone due to the decreased total electric resistance (since the averaged cross-section section increases with contraction zone shortened). Thus the electric field, electric-field gradient, and the Deborah number near the small end increase with decreasing the length of the contraction zone. However, the accumulated strain still slightly increases with increasing the length of the contraction zone due to the increased integral path, which compensates the loss of the electric-field gradient.

Curves of averaged fractional visual length vs center-of-mass location are shown in Fig. 6(c). Channel no. 2 again achieves the highest stretching due to the highest Deborah number and accumulated strain. Channel no. 1 has the lowest stretching due to its lowest Deborah number although its accumulated strain is just slightly higher than that in channels no. 3 and no. 4. However, this does not mean that the

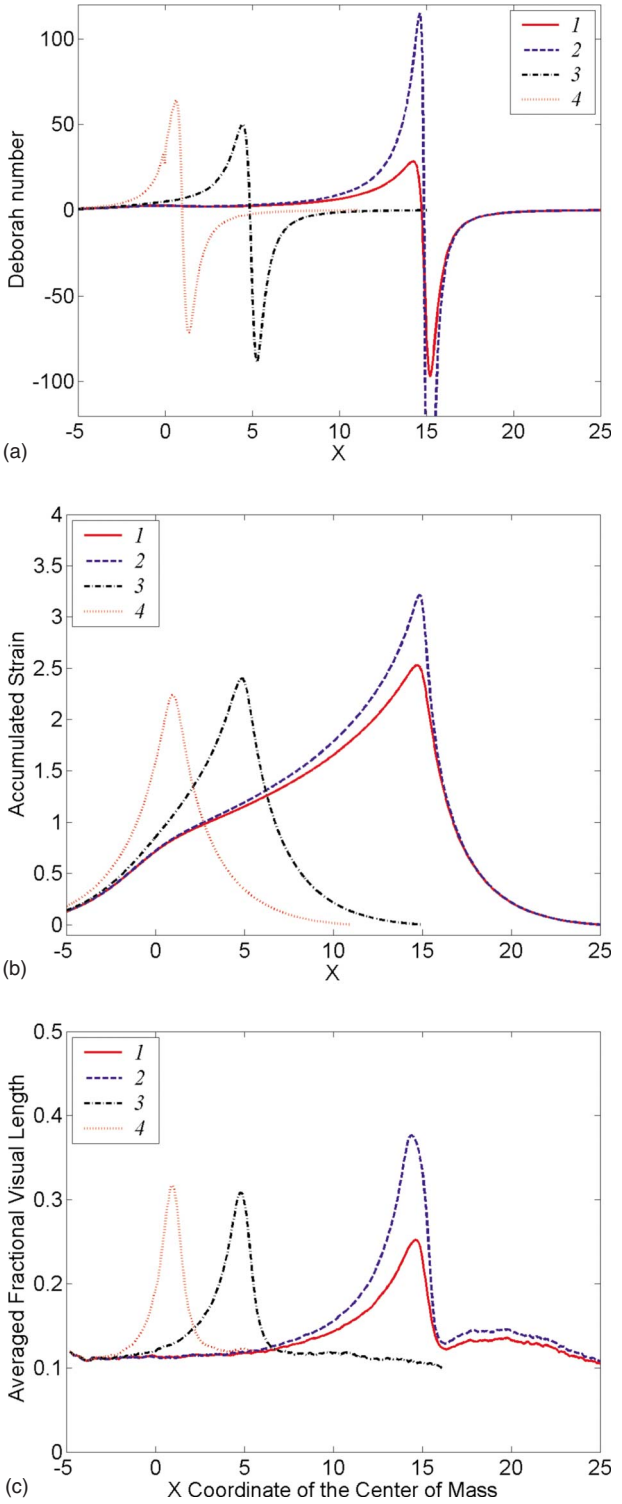

FIG. 6. (Color online) (a) Location-dependent Deborah number and (b) path-dependent accumulated strain vs x-axis coordinate along the center lines in channels 1, 2, 3, and 4; (c) the averaged fractional visual length vs the center-of-mass locations of DNA molecules in these four channels.

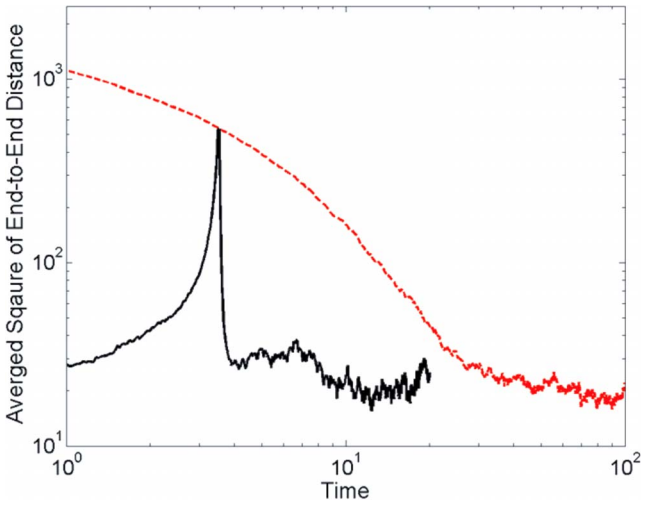

FIG. 7. (Color online) Comparison of forced relaxation and free relaxation.

shorter contraction zone can produce larger stretching. In fact, the length of the contraction zone in Channel no. 4 is 20 μm, almost the same length of the contour length of a YOYO-1 dyed λ-DNA molecule (21 μm). The length of the contraction zone cannot be too small compared with the contour length of DNA molecules; otherwise, the stretching of DNA molecules is limited by the highly decreased accumulated strain, or DNA molecules do not have enough time to be further stretched. From the simulation, decreasing the small-end width can be an effective way to increase the stretching amount. When the small-end width is comparable to the Kuhn step length of a DNA molecule, we need to consider the hydrodynamic interaction between the solid wall and DNA chains [36–42].

E. Free relaxation vs forced relaxation

Electrophoretic dynamics of DNA molecules in contraction-expansion microchannel is quite different from that in the bulk. The stretching relaxation in contraction-expansion microchannel is due to the fast transition of electric-field gradient. Thus we call this relaxation the forced relaxation in order to distinct it from the free relaxation (without any external force) in the bulk. Figure 7 shows the comparison of the ensemble average of square of end-to-end distance $\langle \mathbf{r}_{e-e}^2 \rangle$ vs dimensionless time for both the free relaxation (dashed curve) and forced relaxation (solid curve, Pe $=-84000$; the initial location of DNA molecules are along the center line). Here the forced relaxation curve was shifted horizontally in order to get the same end-to-end distance as the free relaxation at a dimensionless time around 3.5. The free relaxation curve was obtained by averaging the relaxation processes of 100 DNA chains, which initially were uniformly stretched to a straight line with the size at 99% of its full length. From the figure, we can see that it takes 7 unit time for the forced relaxation to reach the equilibrium state, while the free relaxation requires 97 unit time. Thus the forced relaxation due to the reverse compression in the expansion zone (as mentioned in Sec. III B) can speed up the relaxation of DNA molecules. It is worth to mention that a DNA molecule is still partially stretched in the beginning of the forced relaxation because part of its segments is in the contraction zone.

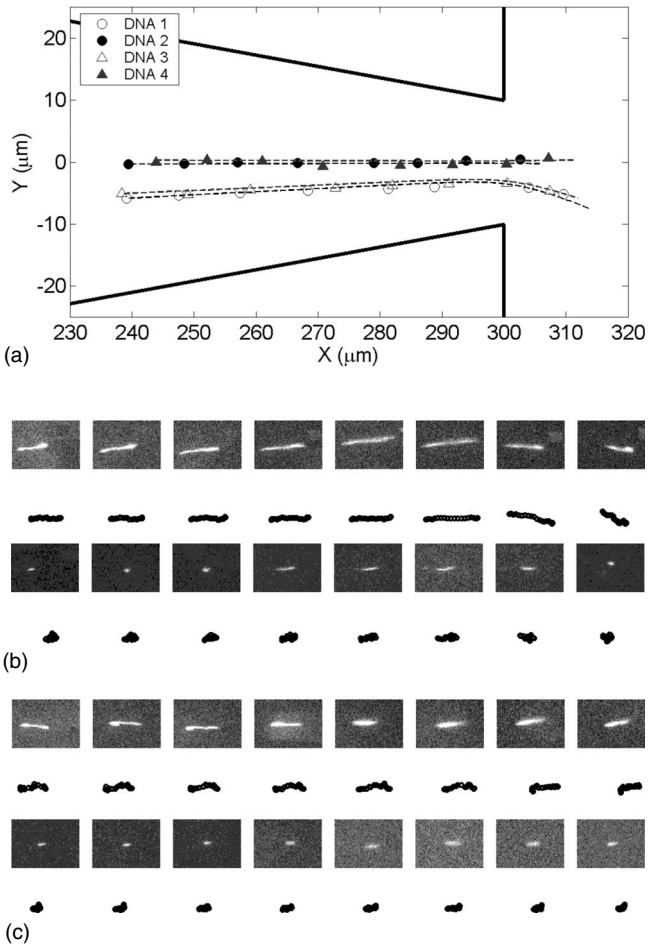

FIG. 8. (a) Trajectories of center-of-mass locations of four DNA chains and corresponding electric-field lines; (b) comparison of experiment and simulation results for the coil-stretch-recoil dynamics of DNAs 1 and 3; (c) comparison of experiment and simulation results for the coil-stretch-recoil dynamics of DNAs 2 and 4.

F. Comparison between experiment and simulation

The coil-stretching-recoil transition of DNA molecules can be verified by experimental observations [34] (detailed information on experiment setups and preparation can also be found in the supplemental materials [35]). In order to clearly observe fluorescent DNA molecules under the microscope, we used a 100× camera and a snapshot covering on an area of around 90 μm by 58 μm. In Fig. 8, there are four different DNA molecules particularly chosen from a large number of DNA molecules taken in our experimental videos. Trajectories of DNAs 1 and 3 are very close to the central line, while DNA chains 2 and 4 are closer to the lower wall. The center-of-mass locations of these DNA molecules are represented by four different symbols in Fig. 8(a). We can see that center of trajectories of DNA chains overlap with the corresponding electric-field lines. Figures 8(b) and 8(c) show

the comparison between experiments and simulation on DNA electrophoretic dynamics in contraction-expansion microchannel. By choosing the bead-spring chain with the similar initial configuration and the initial center-of-mass location at the electric-field strength Pe=−21000 in the simulation, we can achieve good qualitative agreement (similar configurations and visual length) with experimental results.

In Fig. 8(b), initially DNA 1 is partially stretched (visual length around 9.1 μm) in the contraction zone and the electric-field gradient continues to stretch it until it reaches the small end of the contraction zone for a length around 15 μm. Then the DNA molecule is quickly compressed back to the folded shape with a length close to 8 μm when it moves out of the contraction zone. DNA 3, on the other hand, starts with a coiled shape and is barely stretched to a length around 5 μm after experiencing the same distance in the contraction zone. It takes less time to recoil back to its equilibrium state than DNA 1. In Fig. 8(c), we find a similar behavior for DNAs 2 and 4. For DNA 2, its visual length just slightly changes from 8.6 to 9.6 μm, then coils back to 6.8 μm. DNA 4 is slightly stretched to a length of 3.5 μm at the small end before it recoils back. Thus it again shows that the effect of initial configuration is very important for the behavior of DNA chains at a fixed external electric field.

IV. CONCLUSIONS

In summary, we have numerically studied DNA dynamics in different tapered contraction-expansion microchannels and compared one with the experimental observations. Tapered contraction-expansion channels can produce high electric field and gradient. This unique characteristic can be used to accelerate and stretch DNA molecules inside the contraction zone and speed the relaxation or compression of DNA molecules in the expansion zone. The possible applications of the contraction-expansion microchannel may include gene delivery to cells and the electrophoretic separation of large DNA molecules.

DNA dynamics in a specified tapered contraction-expansion microchannel driven by the electrophoretic force is affected by three important factors, i.e., the initial configuration of DNA chains, the initial center-of-mass location, and the external electric-field strength. DNA chains display a large discrepancy in their behaviors at the same initial location and electric-field strength is mainly due to the wide distribution of their initial configurations. Different behaviors of DNA chains with different initial location and electric-field strength can eventually contribute to the path-dependent accumulated strain and location-dependent Deborah number. The combination of FEM simulation and Brownian dynamics simulation is successful in the study of DNA dynamics in the contraction-expansion microchannels and the simulation is in good agreement with experiments.

ACKNOWLEDGMENTS

The authors are grateful to Professor Ron G. Larson at University of Michigan for helpful discussion. This work was partially supported by the National Science Foundation sponsored Nanoscale Science and Engineering Center for Affordable Nanoengineering of Polymeric Biomedical Devices (Grant No. EEC-0425626).

[1] T. T. Perkins, D. E. Smith, and S. Chu, Science **264**, 819 (1994).
[2] S. B. Smith, L. Finzi, and C. Bustamante, Science **258**, 1122 (1992).
[3] H. G. Hansma, Annu. Rev. Phys. Chem. **52**, 71 (2001).
[4] T. T. Perkins, D. E. Smith, and S. Chu, Science **276**, 2016 (1997).
[5] D. E. Smith and S. Chu, Science **281**, 1335 (1998).
[6] G. C. Randall and P. S. Doyle, Phys. Rev. Lett. **93**, 058102 (2004).
[7] Y.-J. Juang, S. Wang, X. Hu, and L. J. Lee, Phys. Rev. Lett. **93**, 268105 (2004).
[8] A. D. Stroock, M. Weck, D. T. Chiu, W. T. S. Huck, P. J. A. Kenis, R. F. Ismagilov, and G. M. Whitesides, Phys. Rev. Lett. **84**, 3314 (2000).
[9] Y.-J. Juang, X. Hu, S. Wang, L. J. Lee, C. Lu, and J. Guan, Appl. Phys. Lett. **87**, 244105 (2005).
[10] X. Hu, S. Wang, Y.-J. Juang, and L. J. Lee, Appl. Phys. Lett. **89**, 084101 (2006).
[11] J. Han and H. G. Craighead, Science **288**, 1026 (2000).
[12] M. Streek, F. Schmid, T. T. Duong, and A. Ros, J. Biotechnol. **112**, 79 (2004).
[13] A. S. Panwar and S. Kumar, Macromolecules **39**, 1279 (2006).
[14] M. Streek, F. Schmid, T. T. Duong, D. Anselmetti, and A. Ros, Phys. Rev. E **71**, 011905 (2005).
[15] G. C. Randall, K. M. Schultz, and P. S. Doyle, Lab Chip **6**, 516 (2006).
[16] J. M. Kim and P. S. Doyle, Lab Chip **7**, 213 (2007).
[17] R. G. Larson, T. T. Perkins, D. E. Smith, and S. Chu, Phys. Rev. E **55**, 1794 (1997).
[18] R. G. Larson, H. Hu, D. E. Smith, and S. Chu, J. Rheol. **43**, 267 (1999).
[19] R. G. Larson, J. Rheol. **49**, 1 (2005).
[20] P. S. Doyle and E. S. G. Shaqfeh, J. Non-Newt. Fluid Mech. **76**, 43 (1998).
[21] J. S. Hur, E. S. G. Shaqfeh, and R. G. Larson, J. Rheol. **44**, 713 (2000).
[22] A. S. Panwar and S. Kumar, J. Chem. Phys. **118**, 925 (2003).
[23] E. S. G. Shaqfeh, J. Non-Newt. Fluid Mech. **130**, 1 (2005).
[24] N. J. Woo, E. S. G. Shaqfeh, and B. Khomami, J. Rheol. **48**, 281 (2004).
[25] N. J. Woo, E. S. G. Shaqfeh, and B. Khomami, J. Rheol. **48**, 299 (2004).
[26] C. Bustamante, J. F. Marko, E. D. Siggia, and S. Smith, Science **265**, 1599 (1994).
[27] J. F. Marko and E. D. Siggia, Macromolecules **28**, 8759 (1995).
[28] M. Somasi, B. Khomami, N. J. Woo, J. S. Hur, and E. S. G.

Shaqfeh, J. Non-Newt. Fluid Mech. **108**, 227 (2002).
[29] X. Hu, Ph.D. thesis, The Ohio State University, 2006.
[30] D. R. Baker, *Capillary Electrophoresis* (Wiley, New York, 1995).
[31] R. Kuhn and S. Hoffstetter-Kuhn, *Capillary Electrophoresis: Principles and Practice* (Springer-Verlag, Berlin, Germany, 1993).
[32] J. C. Heinrich and D. W. Pepper, *Intermediate Finite Element Method: Fluid Flow and Heat Transfer Applications* (Taylor & Francis, Philadelphia, PA, 1999).
[33] R. Lohner, *Applied CFD Techniques: An Introduction Based on Finite Element Methods* (Wiley, New York, NY, 2001).
[34] S. Wang, Ph.D. thesis, The Ohio State University, 2006.
[35] See EPAPS Document No. E-PLEEE8-79-052904 for details of experimental setup and simulations. For more information on EPAPS, see http://www.aip.org/pubservs/epaps.html.
[36] C.-C. Hsieh, L. Li, and R. G. Larson, J. Non-Newt. Fluid Mech. **113**, 147 (2003).
[37] L. Fang, H. Hu, and R. G. Larson, J. Rheol. **49**, 127 (2005).
[38] R. M. Jendrejack, E. T. Dimalanta, D. C. Schwartz, M. D. Graham, and J. J. de Pablo, Phys. Rev. Lett. **91**, 038102 (2003).
[39] R. M. Jendrejack, D. C. Schwartz, M. D. Graham, and J. J. de Pablo, J. Chem. Phys. **119**, 1165 (2003).
[40] H. Ma and M. D. Graham, Phys. Fluids **17**, 083103 (2005).
[41] N. Watari, M. Makino, N. Kikuchi, R. G. Larson, and M. Doi, J. Chem. Phys. **126**, 094902 (2007).
[42] Y.-L. Chen, H. Ma, M. D. Graham, and J. J. de Pablo, Macromolecules **40**, 5978 (2007).